Supplementary Information

Boosting Alkaline Hydrogen Evolution: Dominating Role of Interior Modification in Surface Electrocatalysis

Zhao Li[1,2,#], Wenhan Niu[2,#], Zhenzhong Yang[3,#], Abdelkader Kara[4,7], Qi Wang[5], Maoyu Wang[6], Meng Gu[5,], Zhenxing Feng[6,*], Yingge Du[3,*], and Yang Yang[1,2,7,*]*

[1]*Department of Materials Science and Engineering, University of Central Florida, Orlando, FL 32826, United States*

[2]*NanoScience Technology Center, University of Central Florida, Orlando, FL 32826, United States*

[3]*Physical and Computational Sciences Directorate, Pacific Northwest National Laboratory, Richland, Washington 99352, United States*

[4]*Department of Physics, University of Central Florida, Orlando, FL 32826, United States*

[5]*Department of Materials Science and Engineering, Southern University of Science and Technology, Shenzhen 518055, China*

[6]*School of Chemical, Biological, and Environmental Engineering, Oregon State University, Corvallis, OR 97331, United States*

[7]*Energy Conversion and Propulsion Cluster, University of Central Florida, Orlando, FL 32826, United States*

[*]*Email: gum@sustc.edu.cn; zhenxing.feng@oregonstate.edu; Yingge.Du@pnnl.gov; Yang.Yang@ucf.edu*

[#] *These authors contributed equally to this work.*

Experimental Section

Chemicals: Sulfuric acid (H_2SO_4, 95-98%, Sigma-Aldrich), potassium hydroxide (KOH, ≥85%, Sigma-Aldrich), sodium hypophosphite monohydrate ($NaH_2PO_2 \cdot H_2O$, ≥99%, Sigma-Aldrich), dihydrogen hexachloroplatinate (IV) hydrate ($H_2PtCl_6 \cdot 7H_2O$, ≥99.9%, Alfa Aesar), cobalt (II) sulfate heptahydrate ($CoSO_4 \cdot 7H_2O$, 98%, Alfa Aesar), nickel sulfate hexahydrate ($NiSO_4 \cdot 6H_2O$, certified, Fisher Chemcial), zinc sulfate heptahydroate ($ZnSO_4 \cdot 7H_2O$, certified, Fisher Chemical), sodium tungstate dihydrate ($Na_2O_4W \cdot 2H_2O$, 99%, Acros Organics), sodium dodecyl sulfate ($C_{12}H_{25}NaO_4S$, >99%, Biosciences), sodium citrate dihydrate ($Na_3C_6H_5O_7 \cdot 2H_2O$, granular certified, Sigma-Aldrich), boric acid (H_3BO_3, ≥99.5%, Fisher Chemical), sodium chloride (NaCl, 99-100.5%, Fisher Chemical), sulfuric acid (H_2SO_4, certified, Fisher Chemcial), perchloric acid ($HClO_4$, certified, Fisher Chemical), platinum on carbon (Pt/C, 10 wt% loading, Sigma-Aldrich), isopropanol (C_3H_8O, ≥99.5%, Fisher Chemical) and carbon cloth (Fuel Cell Earth) were used as received.

The fabrication process for Pt-Co_2P supported on carbon cloth (CC): H_3BO_3 (30 g L^{-1}), $Na_3C_6H_5O_7 \cdot 2H_2O$ (15 g L^{-1}), and $C_{12}H_{25}NaO_4S$ (1 g L^{-1}) were mixed with $CoSO_4 \cdot 7H_2O$ (115 g L^{-1}) in deionized (DI) water and then added 2 mM $H_2PtCl_6 \cdot 7H_2O$ stirring for 10 min. The bottom-up electrodeposition was conducted by using CC as the cathode and platinum mesh as the anode, keeping 1 h under 0.1 A. The as-prepared PtCo alloy was phosphorized under 300 °C for 2 h by using $NaH_2PO_2 \cdot H_2O$, Finally, it was cleaned by dilute H_2SO_4 and DI water drying under room temperature. Note that NaH_2PO_2 was decomposed to PH_3, consequently producing P-atoms during

the thermal treatment. As the result of the diffusion limitation, usually occurring in the top-down phosphatization reaction under CVD treatment, a concentration gradient of P and the formation of the P-rich outer layer was achieved.[1-4]

The fabrication process of Co_2P and Pt@Co_2P supported on carbon cloth (CC): The same electrodeposition solution but without $H_2PtCl_6 \cdot 7H_2O$ were prepared for bottom-up electrodeposition under 0.1 A for 1h. Then the precursor supported on CC was phosphorized under 300 °C for 2 h and cleaned by dilute H_2SO_4 and DI water drying under room temperature. After that, Co_2P supported on CC was well-prepared. Finally, the second electrodeposition was carried out under the mixed solution including H_3BO_3 (30 g L^{-1}), $Na_3C_6H_5O_7 \cdot 2H_2O$ (15 g L^{-1}), $C_{12}H_{25}NaO_4S$ (1 g L^{-1}) and 2 mM $H_2PtCl_6 \cdot 7H_2O$ for 1h under 0.1 A. The Pt@Co_2P was successfully prepared for usage.

Fabrication of Pt/C on CC: The Pt/C supported on CC as the control sample was prepared by dispersing the as-prepared solution including Pt/C powder, DI water, Nafion and isopropanol, and then dried in the oven for 1h at 60 ºC.

Materials characterizations: The morphology and composition were investigated by a high-resolution transmission electron microscope (HRTEM) with energy-dispersive X-ray spectroscopy (EDS) mapping (Cs-corrected JEM ARM200F STEM and FEI Titan 80-300 S/TEM operating at 200 kV and 300 kV, respectively) together with scanning electron microscopy (SEM, ZEISS ultra 55). The crystal structure was characterized by X-ray diffraction (XRD) instrument (Panalytical X'celerator multi-element detector with Cu Kα radiation source, λ=1.54056 Å). The electronic structures and chemical states of the composition were characterized by X-ray photoelectron

spectroscopy (XPS Escalab 250Xi). X-ray fluorescence spectrometer (XRF, PANalytical Epsilon) and inductively coupled plasma mass spectroscopy (Agilent, 7770X) were employed to analyze the chemical component. Pt L-edge and Co K-edge X-ray absorption near edge structure (XANES) and extended X-ray absorption fine structure (EXAFS) experiments were carried out at beamline 5BM-DND-CAT, Advanced Photon Source (APS), Argonne National Laboratory (ANL). Data reduction, data analysis, and EXAFS fitting were performed with the Athena, Artemis, and IFEFFIT software packages.

Electrochemical characterizations: All the electrochemical measurements were measured in a three-electrode cell, including the reference electrode (Ag/AgCl, 1 M KCl), the counter electrode (carbon rod) and the working electrode (the as-prepared catalysts supported on CC), which was tested by the electrochemical station (CHI 760E). All the measured potentials with Ag/AgCl electrode as the reference were converted into reversible hydrogen electrode (RHE) by the equation $E_{RHE} = E_{Ag/AgCl} + 0.059\ pH + 0.222$. The calibration of the reference electrode was conducted in the H_2-saturated 1 M KOH solution with Pt foils as the working and counter electrodes at a scan rate of 5 mV s^{-1}. All the Hydrogen evolution reaction (HER) polarization curves were iR-corrected.

The active site density was estimated in the Ar-saturated electrolyte containing 0.5 M H_2SO_4, 20 mM $CuSO_4$, and 60 mM NaCl at a scan rate of 2 mV s^{-1}, according to the underpotential deposition (UPD) method. The molar of electrodeposited Cu from UPD and the corresponding density of active sites were calculated by the equation of $n = Q_{Cu}/2F$ and $q = n \times N_A$, where the n, Q_{Cu}, F, q, and N_A are the molar amount of deposited Cu, the charge quantity produced during the

Cu stripping process, the Faraday constant, the density of active sites, and Avogadro's constant, respectively. The turnover frequency (TOF) was measured by the equation of TOF = j/q (1.602×10^{-19}) × 2, where j is the current density.

The cyclic and linear sweep voltammetry (CV and LSV) was measured at 5 mV s^{-1}. Electrochemical impedance spectroscopy (EIS) was recorded in the frequency range from 1×10^{6} to 0.01 Hz at different overpotentials. The electrical double-layered capacitance (C_{dl}) was estimated by CV curves within 0.068 - 0.128V (vs RHE) at different scan rates from 10 mV s^{-1} to 50 mV s^{-1}. Specifically, the electrochemical active surface area (ECSA) is calculated by the equation of ECSA = A × C_{dl}/C_s, where A is the geometric area. The chronopotentiometry curves were investigated at the current density of 100 mA cm^{-2}. The overall water splitting was conducted by a two-electrode system with Pt-Co_2P as the working electrode and carbon rod as the counter electrode at a different current density from 1 to 100 mA cm^{-2}.

Calculations were performed using density functional theory (DFT) using the PBE exchange-correlation functional as implemented in VASP version 5.4.4. The interaction between the valence electrons and ionic cores was described by the projector augmented wave (PAW) method. The plane wave energy cut-off was set to 400 eV. The bulk lattice parameters were determined by allowing the whole cell to relax and using a 12× 6 × 6 sampling of the Brillouin zone. The bulk Co_2P lattice parameters were calculated using a 12 atoms cell (4P-8Co) and we found these parameters to be a= 3.504 Å, b= 5.508 Å, and c= 6.582 Å in good agreement with the experimental values of 3.510 Å, 5.519 Å, and 6.6.591 Å. The threshold for the convergence criteria of 0.02 eV/Å was used for forces convergence. The (100) surface using 32 P atoms and 64 atoms distributed in

4 layers is applied. For the surface calculations, a 2 × 2 × 1 Brillouin zone sampling was used. For the density of states (DOS) calculations, a 6 × 6 × 1 Brillouin sampling was used. For the Pt-Co_2P system, we have put one Pt atom in the subsurface layer for the simulation. For the P-rich surface, we have replaced 8 (out of 16) Co surface atoms by P atoms, reaching a 50/50 stoichiometry. All calculations are spin-polarized.

Supplementary Figures

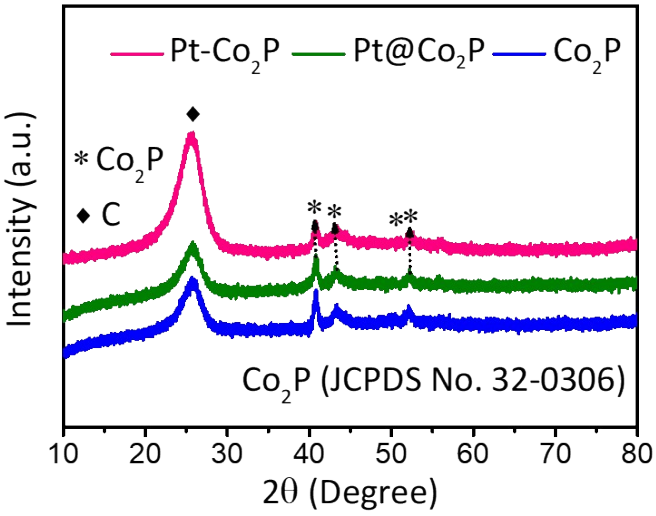

Figure S1. XRD patterns of Pt-Co_2P, Pt@Co_2P, and Co_2P supported on CC, respectively.

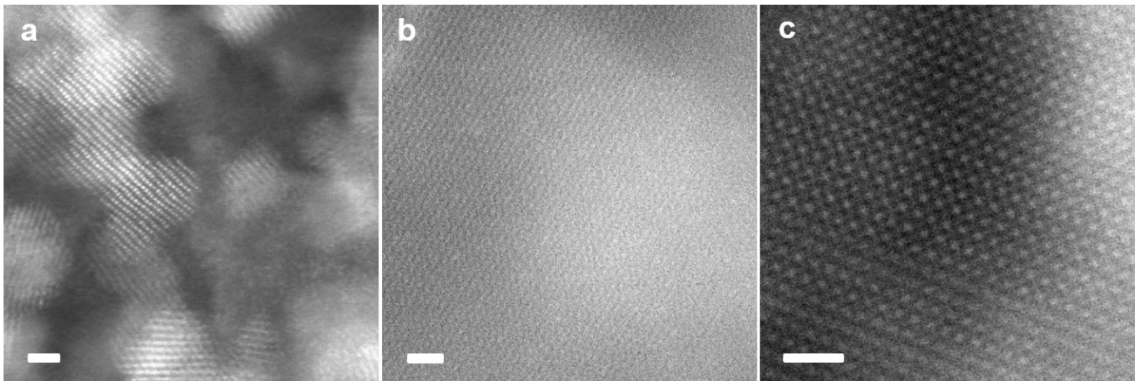

Figure S2. The high-resolution TEM images of (a) Pt@Co_2P and (b,c) Pt-Co_2P. Scale bar: 1 nm.

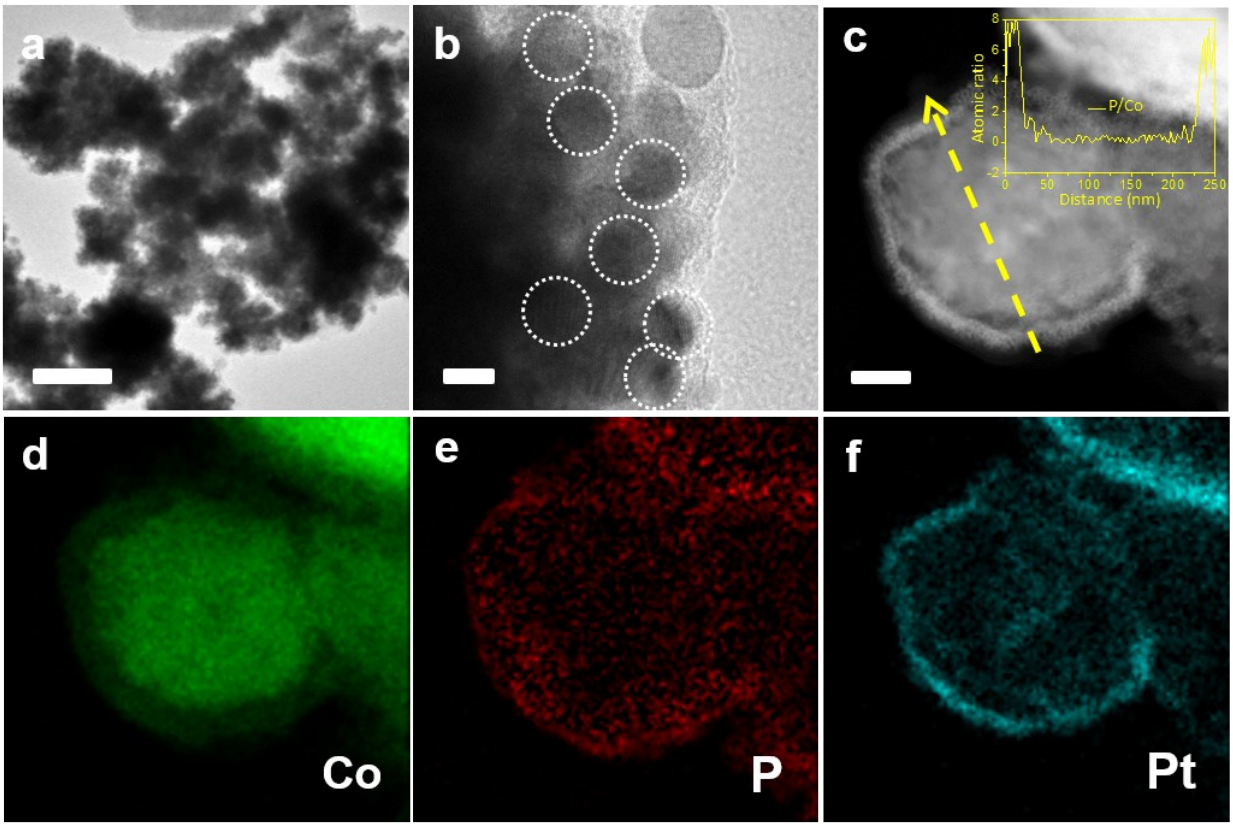

Figure S3. Morphology and composition of Pt@Co_2P. (a, b) TEM images of Pt@Co_2P. Scale bars: 100 nm and 5 nm, respectively. (c) STEM images of Pt@Co_2P including the atomic ratio of P to Co from the EDS line scale. Scale bar: 50 nm. (d-f) STEM-EDS elemental mapping of Pt@Co_2P.

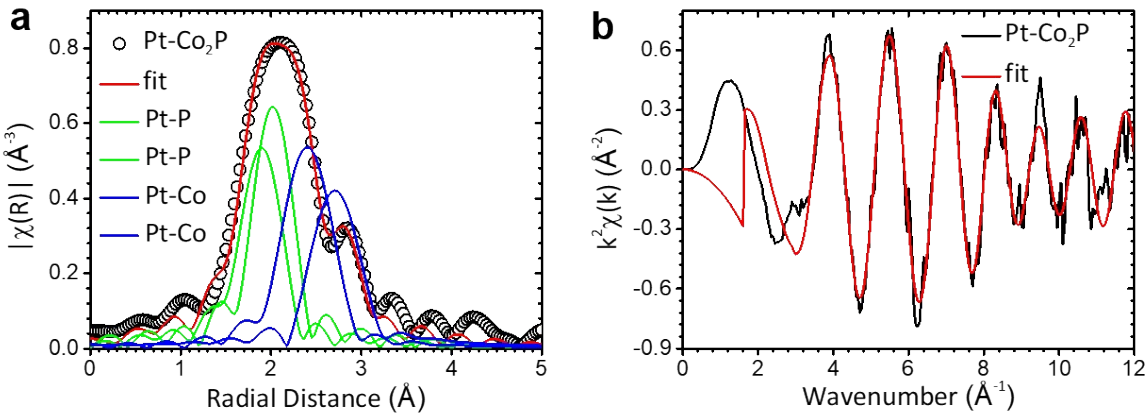

Figure S4. Pt L-edge EXAFS fitting of Fourier Transfer (a) R-space (b) K-space.

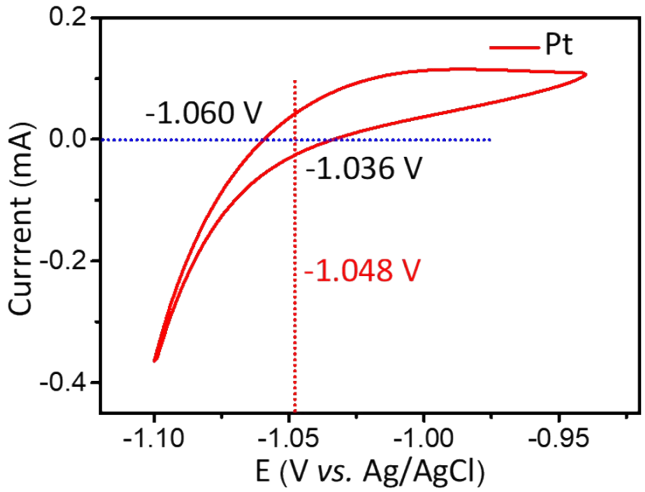

Figure S5. The reversible hydrogen electrode (RHE) voltage calibration.

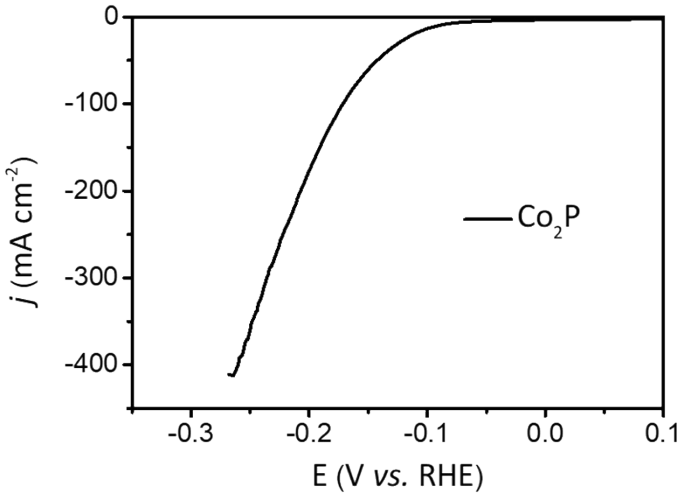

Figure S6. LSV curve of Co_2P.

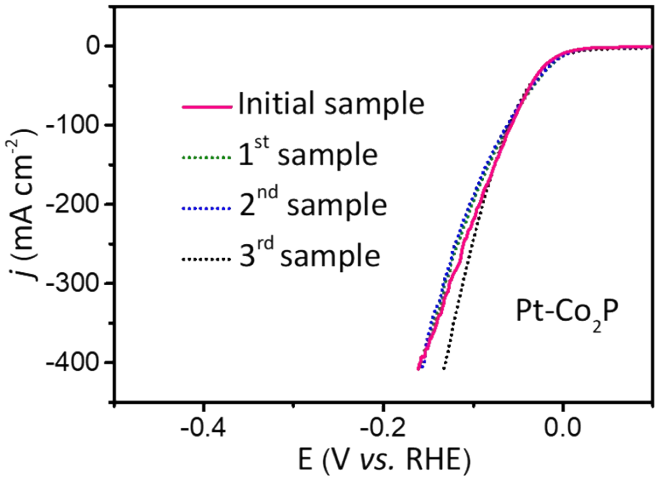

Figure S7. Repeatable performances of HER recorded by using Pt-Co_2P catalysts fabricated at different batches.

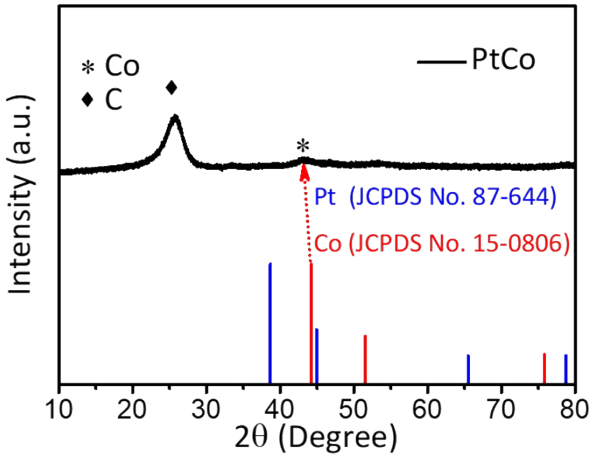

Figure S8. The XRD pattern of PtCo alloy. An obvious peak at 43.37° belongs to the Co (111) plane, which shows a slightly negative shift as compared to the standard PDF card of Co because of the doping effect.

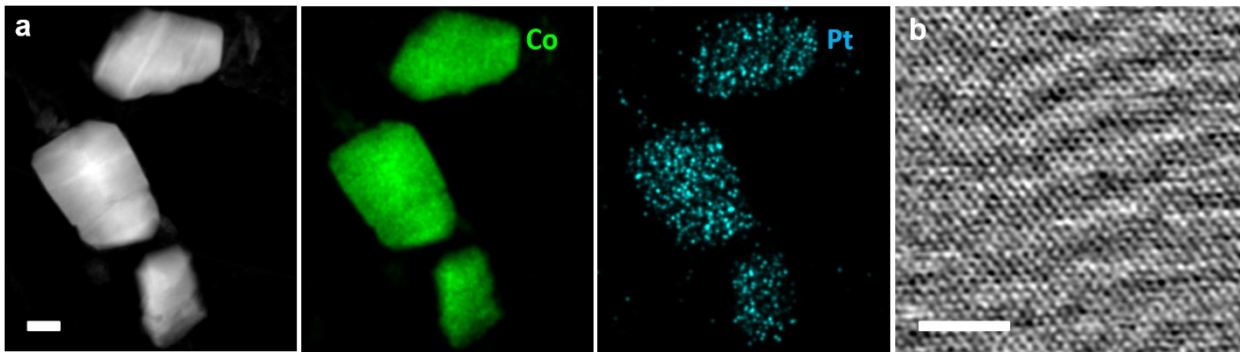

Figure S9. (a) STEM-EDS element mapping, where Pt is uniformly distributed in the whole PtCo matrix and (b) high-resolution TEM images of PtCo alloy. Scale bar: (a) 100 nm and (b) 2 nm.

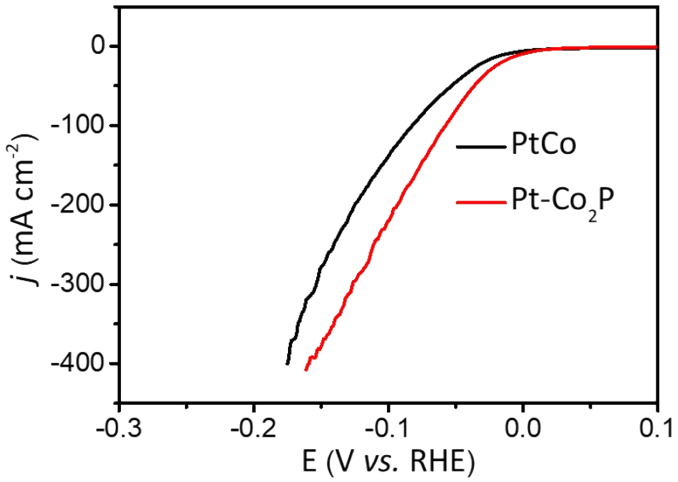

Figure S10. The HER performance of PtCo alloy compared with Pt-Co_2P catalysts.

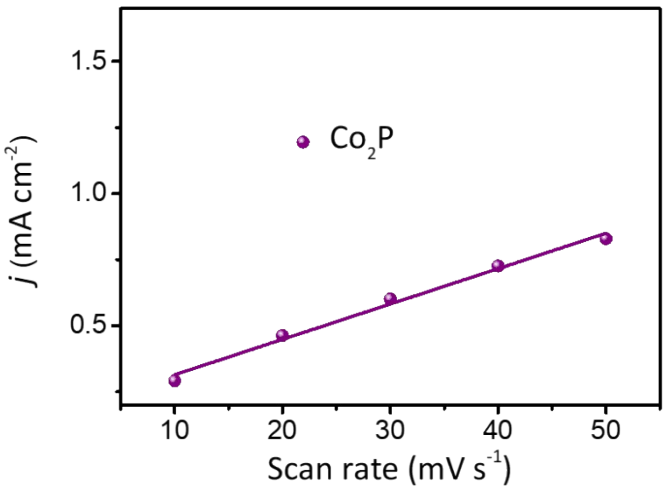

Figure S11. Electrochemical active surface area (ECSA) of Co_2P.

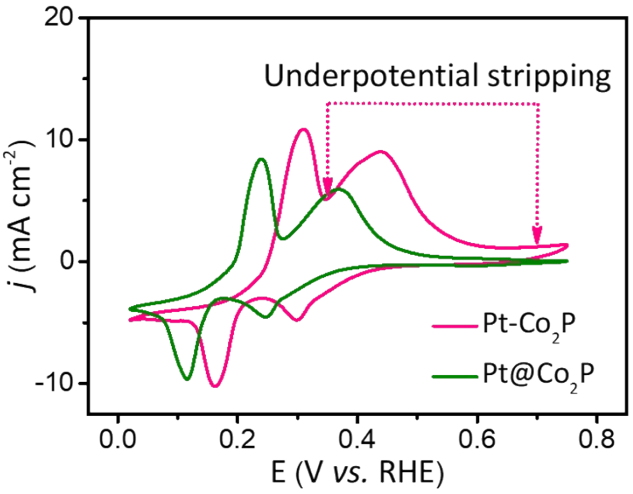

Figure S12. CV measurements of Pt-Co_2P and Pt@Co_2P in Ar-saturated aqueous solution, including 0.5 M H_2SO_4, 20 mM $CuSO_4$, and 60 mM NaCl at a scan rate of 2 mV s^{-1}.

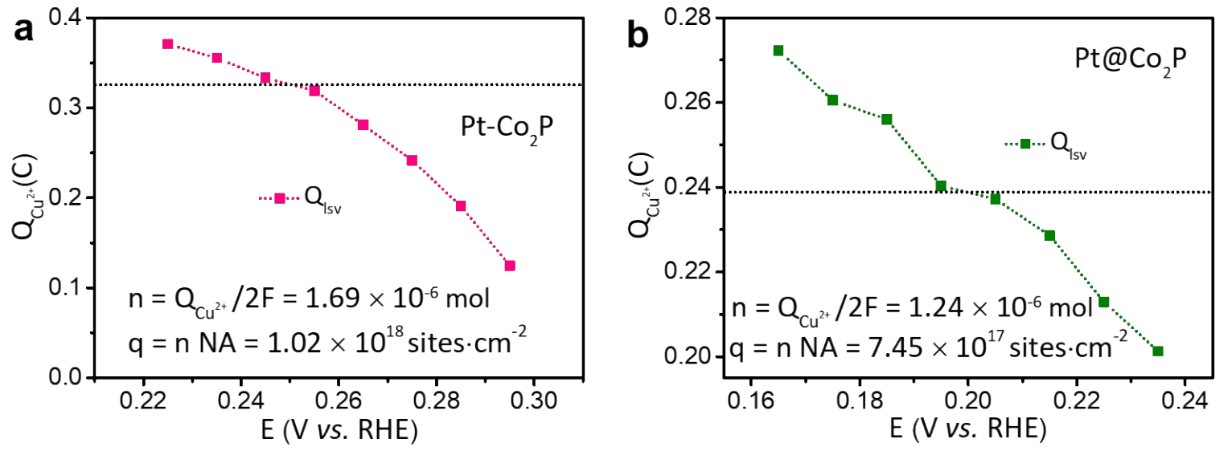

Figure S13. The charges required to strip the Cu deposition at different underpotentials under the UPD method.

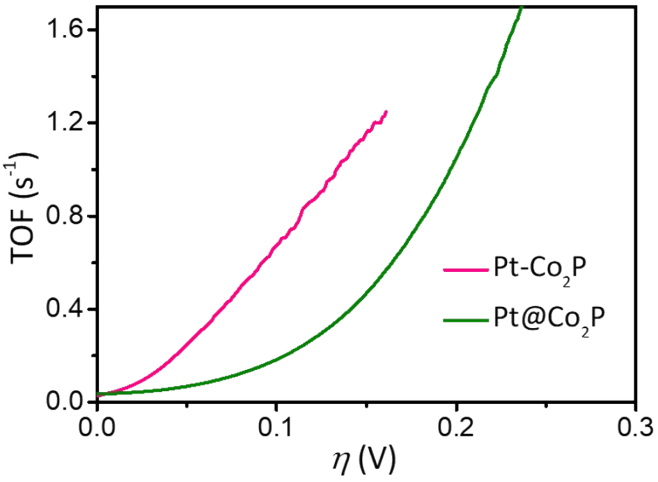

Figure S14. The TOF as a function of overpotential for Pt-Co_2P and Pt@Co_2P.

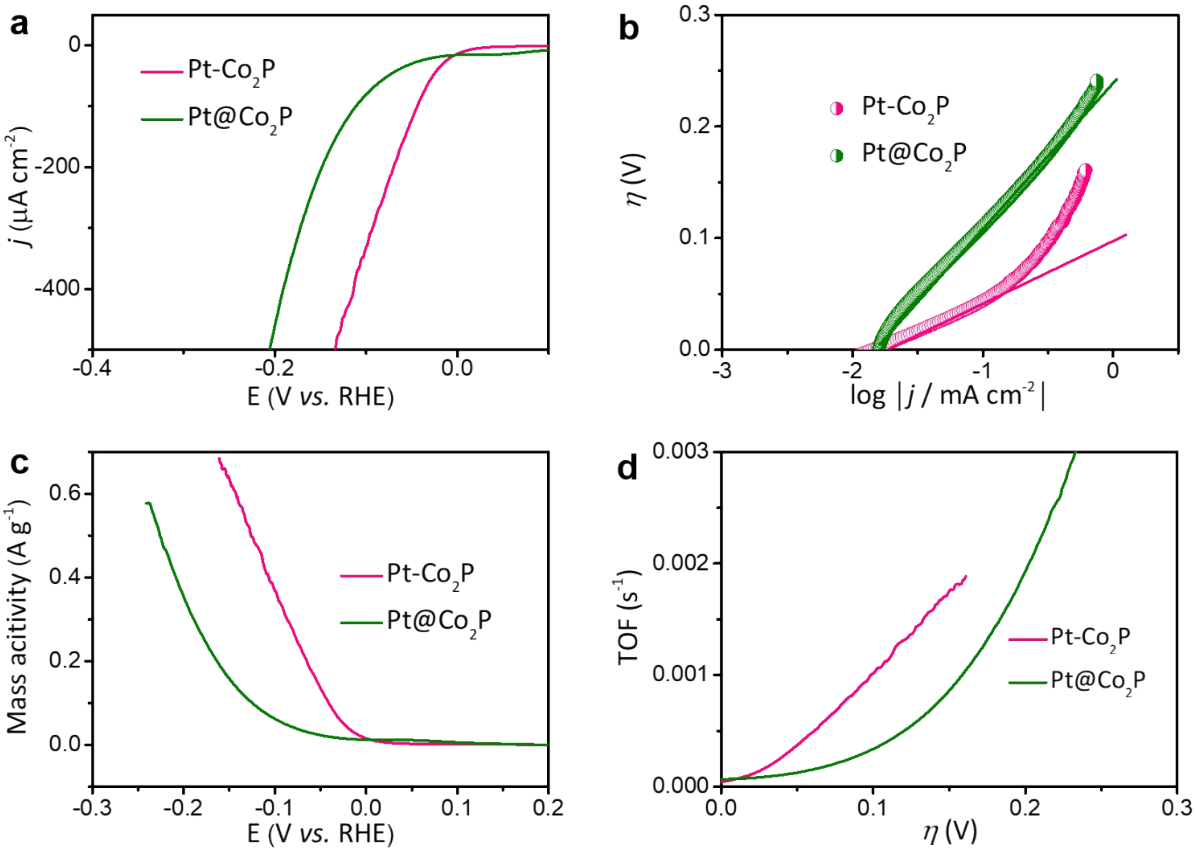

Figure S15. (a) LSV curves, (b) Tafel plots, (c) mass activities, and (d) TOF as a function of overpotential of Pt-Co_2P and Pt@Co_2P normalized by ECSA in 1 M KOH.

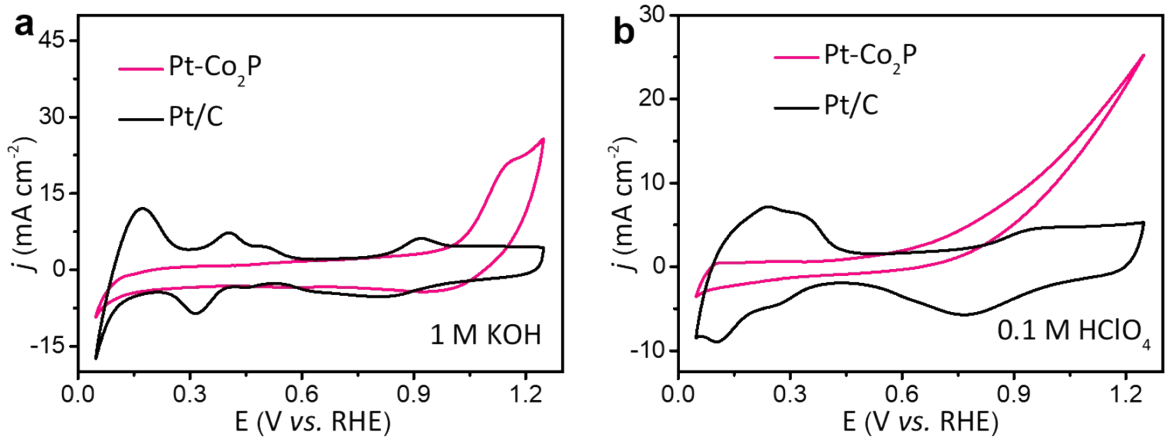

Figure S16. CV curves of Pt-Co_2P and commercial Pt/C in 1 M KOH and 0.1 M $HClO_4$, respectively.

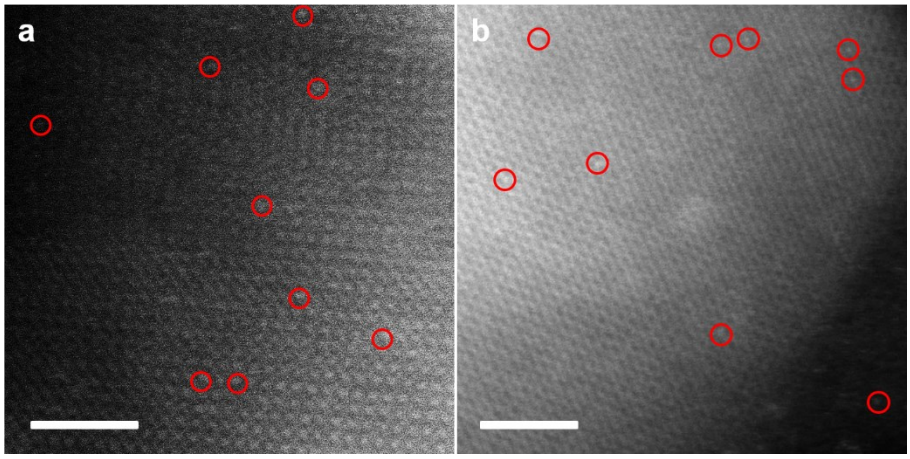

Figure S17. High-resolution TEM image of Pt-Co_2P after stability test. The Pt dopants are stabilized in the lattice of Co_2P as marked by red cycles. Scale bar: 2 nm.

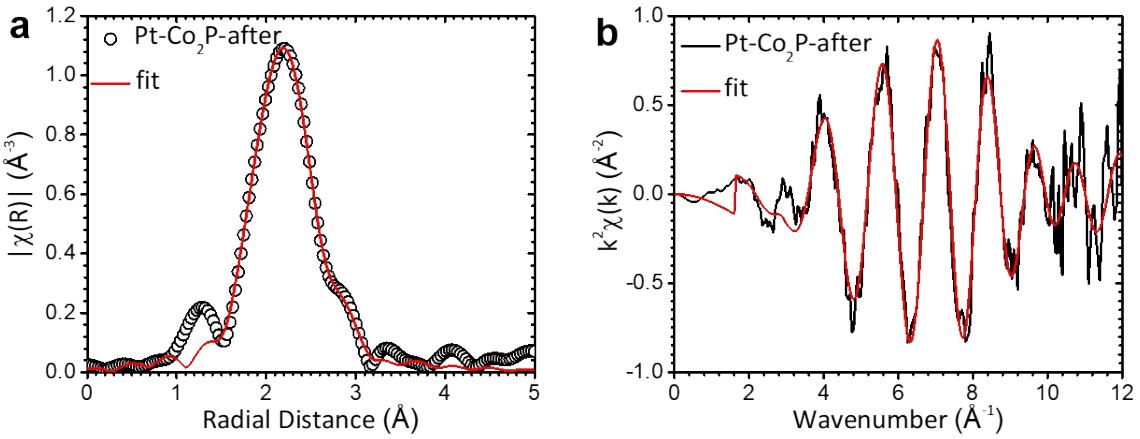

Figure S18. Pt L-edge EXAFS fitting of Fourier Transfer for Pt-Co_2P after stability test (a) R-space (b) K-space.

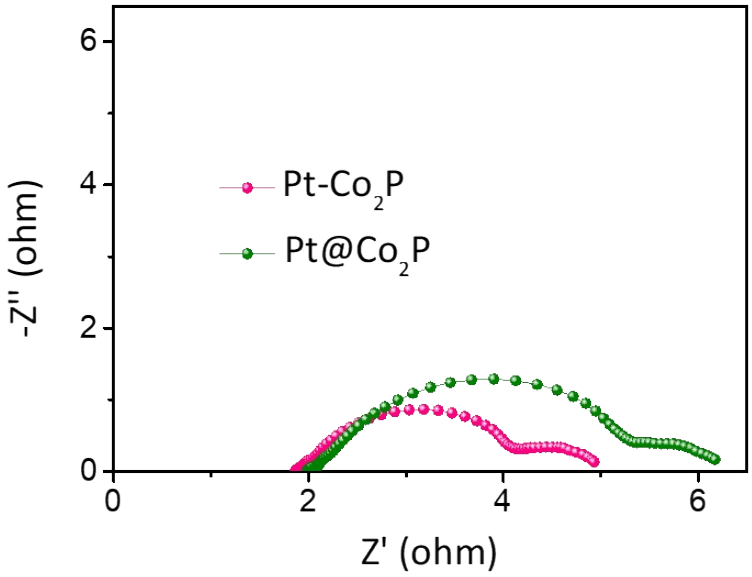

Figure S19. EIS of Pt-Co_2P and Pt@Co_2P at the overpotential of 50 mV.

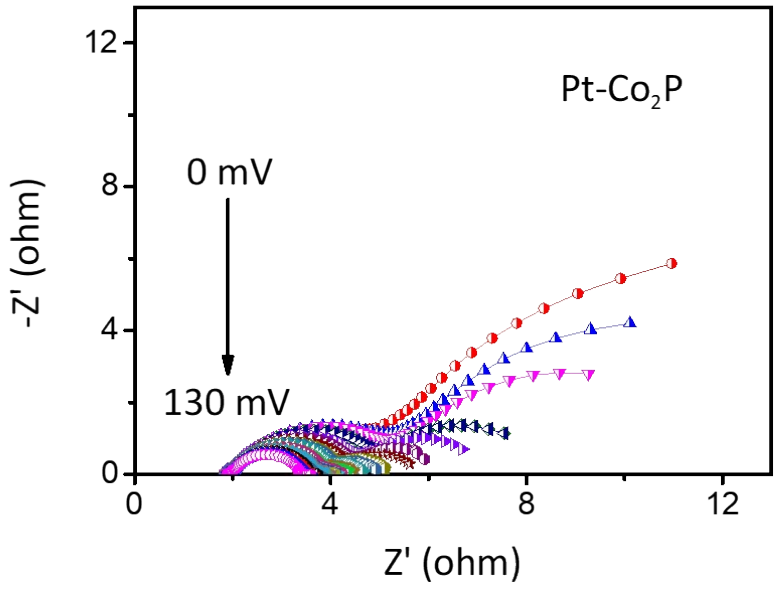

Figure S20. EIS of Pt-Co_2P at the overpotentials from 0 mV to 130 mV.

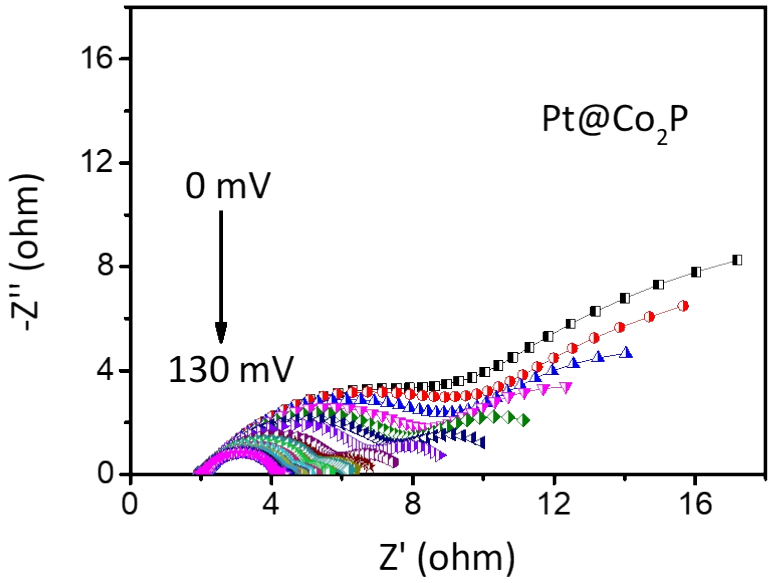

Figure S21. EIS of Pt@Co_2P at the overpotentials from 0 mV to 130 mV.

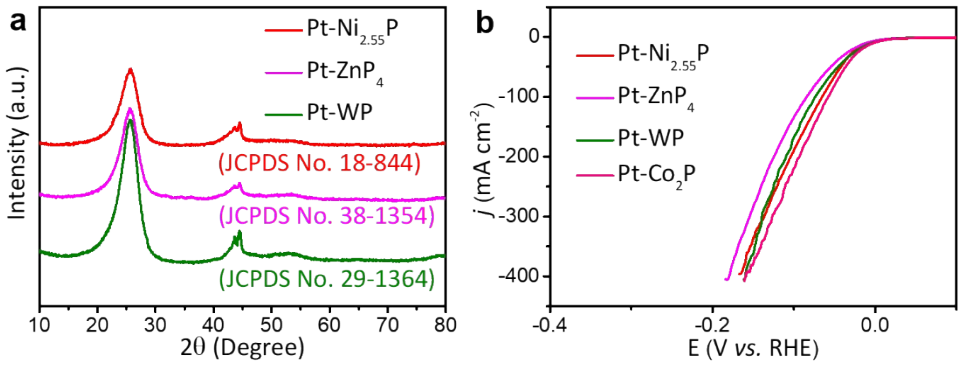

Figure S22. (a) The XRD patterns and (b) A-HER performance of a series catalysts fabricated via a similar method to Pt-Co_2P, including Pt-$Ni_{2.55}P$, Pt-Zn_3P_2, and Pt-WP.

Table S1. The weight percentages of Pt in Pt-Co_2P and Pt@Co_2P measured by XRF and ICP-MS.

Catalyst	Pt weight percentage XRF (wt. %)	Pt weight percentage ICP-MS (wt. %)
Pt-Co_2P	3.58	3.86
Pt@Co_2P	3.60	3.33

Table S2. The atomic ratio of Pt^{2+} and Pt^0 estimated from XPS Pt 4f spectra.

Catalyst	The atomic ratio of Pt^{2+} and Pt^0
Pt-Co_2P	0.40
Pt@Co_2P	0.24

Table S3. The atomic ratio of Co^{2+} and Co^{3+} estimated from XPS Co 2p spectra.

Catalyst	The atomic ratio of Co^{2+} and Co^{3+}
Pt-Co_2P	2.97
Pt@Co_2P	2.14
Co_2P	1.62

Table S4. Fitting parameters of the Pt L-edge EXAFS for Pt-Co_2P (CN: coordination number; R: distance; σ^2: mean-square disorder; E_0: energy shift). The single-digit numbers in parentheses are the last digit errors.

	Scattering Path	CN	R (Å)	E_0 (eV)	σ^2(Å^2)	R-factor	Reduced chi-square
Pt-Co_2P	Pt-P	1.1(1)	2.30(1)	10.0(1)	0.0041(9)	0.02	19.38
	Pt-P	1.1(1)	2.41(2)		0.0008(3)		
	Pt-Co	2.3(2)	2.74(1)		0.0081(2)		
	Pt-Co	1.1(1)	3.02(1)		0.0022(2)		

Table S5. A-HER activities of Pt-Co_2P and the state-of-the-art catalysts.

Catalysts	Onset potential (mV)	η_{10} (mV)	η_{100} (mV)	Electrolyte	Ref.
Pt-Co_2P	**Near-Zero**	**2**	**58**	**1 M KOH**	**This work**
O-Co_2P-3	100	160	233	1 M KOH	[5]
EG-Pt/CoP-1.5	Near-zero	21	108	0.5 M H_2SO_4	[6]
Pt/np-$Co_{0.85}Se$	12	55	-	1.0 M PBS	[7]
CoP_3NAs/CFP	38	126	267	0.5 M H_2SO_4	[8]
Co_2P@NPG	45	103	220	0.5 M H_2SO_4	[9]
Fe-CoP/Ti	20	78	164	1 M KOH	[10]
Pt SA/m-WO_{3-x}	Near-zero	38	-	0.5 M	[11]

				H_2SO_4	
Pt SASs/AG	Near-Zero	12	-	0.5 M H_2SO_4	[12]
IrP_2@NC	Near-Zero	28	-	1 M KOH	[13]
$Pt/Ni(HCO_3)_2$	10	27	116	1 M KOH	[14]

Table S6. Fitting parameters of the Pt L-edge EXAFS for Pt-Co_2P-after after stability performance (CN: coordination number; R: distance; σ^2: mean-square disorder; E_0: energy shift). The single-digit numbers in parentheses are the last digit errors.

	Scattering Path	CN	R (Å)	E_0 (eV)	σ^2(Å^2)	R-factor	Reduced chi-square
Pt-Co_2P-after	Pt-P	1.1(1)	2.35(1)	10.0(1)	0.0008(2)	0.02	9.26
	Pt-P	1.1(1)	2.98(5)		0.0023(6)		
	Pt-Co	2.2(3)	2.66(2)		0.0051(4)		
	Pt-Co	1.1(1)	3.00(3)		0.0021(5)		

Reference

1. X. Xu, J. Liu, R. Hu, J. Liu, L. Ouyang and M. Zhu, *Chem. Eur. J.*, 2017, **23**, 5198-5204.
2. X. Li, W. Liu, M. Zhang, Y. Zhong, Z. Weng, Y. Mi, Y. Zhou, M. Li, J. J. Cha, Z. Tang, H. Jiang, X. Li and H. Wang, *Nano Lett.*, 2017, **17**, 2057-2063.
3. S. Yang, C. Liang and R. Prins, *J. Catal.*, 2006, **237**, 118-130.
4. L. Li, C. Han, L. Yang, X. Wang and B. Zhang, *Ind. Eng. Chem. Res.*, 2010, **49**, 1658-1662.
5. K. Xu, H. Ding, M. Zhang, M. Chen, Z. Hao, L. Zhang, C. Wu and Y. Xie, *Adv. Mater.*, 2017, **29**.
6. J. Li, H.-X. Liu, W. Gou, M. Zhang, Z. Xia, S. Zhang, C.-R. Chang, Y. Ma and Y. Qu, *Energy Environ. Sci.*, 2019, **12**, 2298-2304.
7. K. Jiang, B. Liu, M. Luo, S. Ning, M. Peng, Y. Zhao, Y. R. Lu, T. S. Chan, F. M. F. de Groot and Y. Tan, *Nat. Commun.*, 2019, **10**, 1743.
8. T. Wu, M. Pi, D. Zhang and S. Chen, *J. Mater. Chem. A*, 2016, **4**, 14539-14544.
9. M. Zhuang, X. Ou, Y. Dou, L. Zhang, Q. Zhang, R. Wu, Y. Ding, M. Shao and Z. Luo, *Nano Lett.*, 2016, **16**, 4691-4698.
10. C. Tang, R. Zhang, W. Lu, L. He, X. Jiang, A. M. Asiri and X. Sun, *Adv. Mater.*, 2017, **29**.
11. J. Park, S. Lee, H.-E. Kim, A. Cho, S. Kim, Y. Ye, J. W. Han, H. Lee, J. H. Jang and J. Lee, *Angew. Chem. Int. Ed. Engl.*, 2019, **58**, 16038-16042.
12. S. Ye, F. Luo, Q. Zhang, P. Zhang, T. Xu, Q. Wang, D. He, L. Guo, Y. Zhang, C. He, X. Ouyang, M. Gu, J. Liu and X. Sun, *Energy Environ. Sci.*, 2019, **12**, 1000-1007.
13. Z. Pu, J. Zhao, I. S. Amiinu, W. Li, M. Wang, D. He and S. Mu, *Energy Environ. Sci.*, 2019, **12**, 952-957.
14. M. Lao, K. Rui, G. Zhao, P. Cui, X. Zheng, S. X. Dou and W. Sun, *Angew. Chem. Int. Ed. Engl.*, 2019, **58**, 5432-5437.